High Temperatures-High Pressures, Vol. 54, pp. 533–555
Reprints available directly from the publisher
Photocopying permitted by license only
DOI: 10.32908/hthp.v54.2051

Expressing uncertainty using regression and GUM for derived property measurements based on uncertainty in input quantities

Douglas M. Matson[1*], Jannatun Nawer[1], Kane Bergeron[2] and Brandon Phillips[2]

[1]*Tufts University, Medford MA 02155 USA*
[2]*NASA Marshall Space Flight Center, Huntsville AL 35808 USA*

Received: October 4, 2025; Accepted: November 27, 2025.

In order to validate Integrated Computational Materials Engineering (ICME) thermodynamic property models for high-performance alloy design and advanced manufacturing techniques such as additive manufacturing optimization, it is necessary to quantify the uncertainty during measurement of thermophysical properties of metals and alloys. However, many values reported for these properties in the literature rarely include rigorous uncertainty quantification. The current standard is to report the experimental mean and standard deviation from tabulated experimental data or to plot test results with limited discussion on how error bars are obtained. But this approach does not reveal anything about the underlying systematic or random error propagation. This paper discusses the utility of using a systematic precision-based facility performance evaluation procedure to quantify variability during experimental measurement based on principles developed as part of the Joint Committee for Guides on Metrology (JCGM) *Guide to the Expression of Uncertainty Measurement* (GUM) recommended protocols. Graphical presentation of results is accomplished using a Measurement Accuracy and Precision (MAP) plot where measurement trueness can be evaluated relative to recognized reference value while precision can be assessed by quantification of GUM uncertainties. As an example, the performance of multiple levitation facilities has been successfully compared using these methods for a variety of metallic elements and industrial alloy systems.

Keywords: Measurement uncertainty, regression, derived parameters, thermophysical property

*Corresponding author: jannatun.nawer@tufts.edu

1 INTRODUCTION

In order to model molten metal processing operations such as additive manufacturing, welding, casting, or directional solidification, industry needs to access thermophysical properties across a wide range of commercial alloy systems. A great deal of emphasis is placed on providing experimental data for Integrated Computational Materials Engineering (ICME) thermomechanical based multi-scale Process-Structure-Property-Parameter (PSPP) frameworks. Temperature dependent properties such as density, thermal expansion, viscosity, and surface tension with higher confidence are crucial for PSPP models [1,2]. These models are then used to optimize product quality or guide process control strategies to minimize defect inclusion or to obtain products with superior performance with high reliability [3]. But, in order to fully leverage the use of production model predictions, an understanding of property precision is also of high importance. Users want to understand not only how to optimize performance based on nominal property values based on measurement trueness, but also to understand the potential range of favorable outcomes due to variability and uncertainty in the model input properties, based on precision. [4] Knowing the best-case scenario in a processing window is good, but knowing how robust the process performance is, and how to assess risk mitigation based on model predictions, may dictate the success of any proposed process improvement initiative.

Presentation of the data in most publications is often done in a convenient format with the desired property displayed as a function of temperature. Correlation of results, based on either a linear regression analysis or some physics-based functional relationship, yields a mathematical expression that is readily input into simulations to facilitate modelling activities.

In quantifying property accuracy, both trueness and precision of experimental data, it is important to approach reporting of results in a systematic way. Properties are often derived by measurement of independent quantities that are mathematically combined to obtain the desired values. At high temperature molten metal processing, pyrometry is often used to measure temperature and thus a calibration protocol is often employed. Thus, both variables (the property and the temperature) are derived quantities.

Uncertainty therefore has two components – the quantification of the uncertainty relative to the physics-based functional relationship and the uncertainty in the derived quantities. Uncertainty in the functional relationship component has two contributions. First, there is a description of how well the model performs. For example, with a linear relationship the uncertainty in slope and the uncertainty in intercept may be defined. Second, there is a description of the robustness of the relationship that is developed. For example, how much data scatter exists – basically a quantification of deviation from the fit.

Uncertainty in the derived quantity component also has two contributions. First, there is the uncertainty based on uncertainty in the components used to derive the desired final property. For example, density is based on a measurement of mass and volume, and each has a distinctive associated uncertainty. Second, there is uncertainty in the reported value based on measurement of temperature. Taken together, these two contributions represent the error bars in the ordinate (y-axis) and abscissa (x-axis), respectively. Note that each individual data point may have a unique error bar due to any local variation in test conditions at the time of an individual measurement.

This paper starts by introducing the standard reporting methods used during regression analysis [5] and then concentrates on use of GUM (*Guide to Uncertainty in Measurement*) techniques for characterizing uncertainty in derived quantities [6]. The bulk of the paper then presents a numerical example of how the two methods are combined to obtain an estimate of overall uncertainty using as an example the measurement of density as a function of temperature obtained by containerless processing techniques [7]. In particular, this example illustrates how an investigator may obtain an appreciation of where uncertainty most impacts the final correlation and thus where future efforts to improve the technique may be concentrated. The paper concludes with a brief introduction to a new graphical methodology to allow comparisons of techniques across different experimental platforms or between different classes of candidate materials for a particular application. [8-11]

2 METHODS

Uncertainty in Regression Analysis

The most common approach to reporting uncertainty is through a linear regression analysis–which reports only the uncertainty in slope and intercept and either ignore error bars on x and y quantities or place a scaled generic representation somewhere on the plot. A detailed description of how uncertainty was evaluated is most often missing.

In the discussions contained in the current paper the focus will be limited to a linear regression approach, but non-linear techniques may also be similarly addressed except that instead of reporting a global regression slope, only the local instantaneous slope should be considered. For simplicity, the following discussion assumes a physics-based model involving a linear relationship with slope m and intercept b between the independent variable x and dependent variable y to obtain a relationship in the form:

$$y = m \cdot x + b \tag{1}$$

In general, regression analysis captures goodness-of-fit to the appropriate physics-based model and is accomplished using the following relationships

[5]. Each data point is uniquely identified by an indexing variable i to allow calculation of the slope m, the intercept b and deviation s_m and s_b for slope and intercept, respectively. In the following equations, N is the number of data points, $\overline{x}$ is the average of all x-values and $\hat{y}_i$ is the value of the regression fit function at a point defined by observed values of x_i and y_i.

$$m = \frac{N\sum x_i y_i - \sum x_i \sum y_i}{N\sum x_i^2 - \left(\sum x_i\right)^2} \tag{2}$$

$$b = \frac{\sum y_i - m\sum x_i}{N} \tag{3}$$

$$s_m = \frac{s_{yx}}{\sqrt{\sum\left(x_i - \overline{x}\right)^2}} \tag{4}$$

$$s_b = s_{yx}\sqrt{\frac{1}{N} + \frac{\overline{x}^2}{\sum\left(x_i - \overline{x}\right)^2}} \tag{5}$$

$$s_{yx} = \sqrt{\frac{\sum y_i^2 - b\sum y_i - m\sum x_i y_i}{N-2}} \tag{6}$$

In the special case where physics dictates that the relationship must have an intercept at (0, 0)

$$m = \frac{\sum x_i y_i}{\sum x_i^2} \tag{7}$$

$$s_m = \sqrt{\frac{\sum\left(y_i - \hat{y}_i\right)}{(N-1)\sum x_i^2}} \tag{8}$$

Additionally, in order to capture the uncertainty due to random scatter of data the deviation, σ is evaluated using

$$\sigma = \sqrt{\frac{1}{N}\sum_{i=1}^{N}\left(y_i - \hat{y}_i\right)^2} \tag{9}$$

Uncertainty in Measurement Standards

To evaluate and understand the quality of measurement and provide historical documentation of how the ranges of each quantity value contribute to the

overall uncertainty, the *Evaluation of measurement data-Guide to the Expression of Uncertainty Measurement* (**GUM**) JCGM 100:2008 [6] by the Joint Committee for Guides in Metrology Working Group 1 (JCGM/WG 1) is used to systematically track the contribution from each measured quantity used in deriving a property of interest.

In this protocol, if a derived thermophysical property (y) is not measured directly but rather is a function of $x_1, x_2, \ldots . x_n$ input estimates, assuming each is independent of all others, then the combined standard uncertainty (u_c) can be measured using:

$$y = f\left(x_1, x_2, \ldots . x_n\right) \tag{10}$$

$$u_c\left(y\right) = \sqrt{\sum_{i=1}^{n}\left(\frac{\partial f}{\partial x_i}\right)^2 u^2\left(x_i\right)} \tag{11}$$

Visualization of how this protocol was established can be easily accomplished with a simple example. Consider droplets of water falling into a cup. The input function is the volume of a particular droplet x_i while the derived quantity is the mass of the water in the cup f. Each droplet has some statistical uncertainty in volume which, in turn, contributes to a statistical uncertainty in the cumulative mass. Obviously, the slope of this relationship is equal to the density such that $\partial f / \partial x = \rho$. If the slope is high, uncertainty in the function is quite large even for a small uncertainty in input. If the slope is low, uncertainty in the function is small. At the extreme, if the slope is zero, uncertainty in the function is zero no matter how large or small the uncertainty in the input quantity.

The uncertainty in y due to uncertainty in x, $u_x(y)$, is the product of the slope $\partial f / \partial x$ and the uncertainty in x, $u(x)$ as shown in Equation 12. The result of this product thus ensures that the units of the input function are correctly converted to the proper units for the derived function. On a plot, this represents the local error bars at a specific point and can be visualized as a rectangle centered on the point (x, y) with base $u(x)$ and height $u_x(y)$ with a line crossing the rectangle diagonally representing the local slope.

$$u_x\left(y\right) = \partial f / \partial x \cdot u\left(x\right) \tag{12}$$

Higher order terms from the Taylor expansion can be used in cases where the function y is highly non-linear but for the purposes of this paper, these terms are neglected. For example, density, thermal expansion and surface tension are often quite linear whereas viscosity is not. The treatment described in Equation 11 assumes that each of the input estimates is independent from the

others. When this is not the case, the relationship is modified as shown in Equation 13 where the added term represents the degree of correlation between inputs x_i and x_j. Equation 14 provides an estimate of the degree of correlation using the correlation coefficient r

$$u_c(y) = \sqrt{\sum_{i=1}^{n}\left(\frac{\partial f}{\partial x_i}\right)^2 u^2(x_i) + 2\sum_{i=1}^{N-1}\sum_{j=i+1}^{N}\frac{\partial f}{\partial x_i}\frac{\partial f}{\partial x_j}u(x_i x_j)} \tag{13}$$

$$r(x_i x_j) = \frac{u(x_i x_j)}{u(x_i)\cdot u(x_j)} \tag{14}$$

The Pearson correlation coefficient is used to quantify the degree of correlation between the two quantities. It is dimensionless and a value of $r = 0$ represents two uncorrelated inputs while a value of $r = +1$ represents perfect positive correlation and a value of $r = -1$ represents a perfect negative correlation. Considering the case of two inputs (i and j), combining Equations 13 and 14 in the general case yields Equation 15 while the three limiting cases where $r = 0$, 1, and –1 yield Equations 16, 17 and 18, respectively:

$$u_c(y) = \sqrt{\left(\frac{\partial f}{\partial x_i}\right)^2 u^2(x_i) + \left(\frac{\partial f}{\partial x_j}\right)^2 u^2(x_j) + 2r\left[\frac{\partial f}{\partial x_i}u(x_i)\right]\left[\frac{\partial f}{\partial x_j}u(x_j)\right]} \tag{15}$$

for $r = 0$

$$u_c(y) = \sqrt{\left(\frac{\partial f}{\partial x_i}\right)^2 u^2(x_i) + \left(\frac{\partial f}{\partial x_j}\right)^2 u^2(x_j)} \tag{16}$$

for $r = +1$

$$u_c(y) = \sqrt{\left(\frac{\partial f}{\partial x_i}u(x_i) + \frac{\partial f}{\partial x_j}u(x_j)\right)^2} \tag{17}$$

for $r = -1$

$$u_c(y) = \sqrt{\left(\frac{\partial f}{\partial x_i}u(x_i) - \frac{\partial f}{\partial x_j}u(x_j)\right)^2} \tag{18}$$

As a correlation example in pyrometry there are two possible interpretations in the use of a correlation coefficient to obtain the true temperature T. If the apparent liquidus T_{LA} were to increase, then one option is to expect the apparent temperature reading T_A to increase as well. Although the relationship is not truly linear, over small temperature differences the relative change approaches a constant proportionality and thus it might be appropriate to assume that the correlation coefficient approaches the ideal value of one ($r \rightarrow 1$) and that the two inputs are strongly correlated. However, the

counter-argument is that since the two temperatures are taken during different time intervals then there is no correlation, and it is appropriate to assume $r = 0$. It is usually considered that if two measurements are performed on the same apparatus then the uncertainty components due to measurement resolution are independent but that the components due to the calibration and equipment drift are correlated. Specific experimental conditions dictate which approach is more appropriate.

Two types of standard uncertainties are considered in GUM methodologies. *Type A* involves methods of evaluation of uncertainty by the statistical analysis of a series of observations. An example of *Type A* uncertainty is measurement of a specific sample mass over multiple weightings using a calibrated balance. *Type B* involves methods of evaluation of uncertainty by means other than the statistical analysis of a series of observations. An example of *Type B* uncertainty is relying on a published value for the uncertainty of a specific model of balance which thus approximates the calibration behavior of the balance used above. Both may be important, but the investigator must be vigilant to avoid double-counting of uncertainty.

In order to compare the relative contribution from each uncertainty source, it is reasonable to rely on a dimensionless variable that combines two important statistical measures [5]. The coefficient of variation represents the ratio of the standard deviation of a population to the mean value of that population such that $C = \sigma/\mu$. It thus represents a dimensionless fraction that can be expressed as a percentage allowing comparison between different quantities. For example, when deriving density once we determine the coefficient of variation for each of the quantities, we can determine which of the inputs, mass or volume, controls uncertainty in the final measurement.

Thus, we can express all of the uncertainty equations in the form of a coefficient of variation. As an example, in this format Equation 11 becomes:

$$\frac{u_c(y)}{y} = \sqrt{\frac{1}{y^2}\sum_{i=1}^{n}\left(\frac{\partial y}{\partial x_i}\right)^2 u^2(x_i)} \tag{19}$$

Typical derived quantities

To facilitate modeling of high temperature molten metal processes, knowledge of several common thermophysical properties is often required. For example, looking at the highlighted row in Table 1 representing evaluation of density, several such properties include both directly measured quantities (such as sample mass) and derived quantities (such as sample volume). When conducting density measurements using a containerless technique such as electrostatic levitation [12] the volume of the sample is obtained by first levitating a calibration sphere of known uncertainty in radius and digitally recording a shadow-image of the projected area to obtain the number of pixels/inch for a particular experiment session. The sample to be measured is

then levitated and heated to obtain an image profile as a function of temperature. Thus, when deriving the sample radius, the uncertainty of the calibration sphere dimensions are combined with the uncertainty in the image dimensions while the calibration sphere is levitated, and the uncertainty in the image dimensions of the sample. Note that the uncertainty in sample dimensions is often significantly larger than for the calibration sphere as the former is a molten liquid experiencing translation combined with oscillatory and/or spin induced deformation while the latter is an invariant-shaped spherical solid produced explicitly with highly selective dimensional tolerance to limit error.

TABLE 1
Typical derived quantities measured to support molten metal processing

Thermophysical Property		x_f– functional inputs	x_g– confounding variables
Sample mass	m	x_{scale} precision of scale (%) x_{evap} evaporation loss during test (%)	Preferential evaporation of volatile constituents, contamination/oxidation
Temperature	$T = \left[\left(\frac{1}{T_A}\right) + \left(\frac{1}{T_L} - \frac{1}{T_{LA}}\right)\right]^{-1}$	T_A apparent temperature T_L true measured liquidus T_{LA} apparent liquidus	Emissivity shift due to oxidation, transmissivity shifts due to evaporation, sample stability (pyrometer view factor)
Sample radius	$r = p_{exp}\left[\frac{r_{cal}}{p_{cal}}\right]$	px_{exp} sphere radius in pixels during test px_{cal} sphere radius in pixels during calibration r_{cal} radius of calibration sphere	Deviation from sphericity (don't double-count) Time elapsed since calibration
Volume	$V = \frac{4\pi}{3} r^3$	r radius of sample	Deviation from vertical axis symmetry, image spectral intensity gradient (fade)
Density	$\rho = \frac{m}{V}$	m sample mass at time of test V volume at time of test	Experiment time at temperature (points to average), evaporation
CTE	$\beta = \frac{1}{V}\left(\frac{\partial V}{\partial T}\right)$	T sample temperature V volume at time of test	Experiment time at temperature (points to average)
Surface tension	$\gamma = \frac{3\pi m f^2}{8}$	m sample mass at time of test f observed oscillation frequency	Sample translation/stability, higher mode excitation, sample spin, surface oxides
Viscosity	$\eta = \frac{\rho r^2}{5\tau}$	ρ density r radius of sample τ observed oscillation decay time	Sample translation/stability, higher mode excitation, sample spin, turbulence

3 EXPERIMENTAL RESULTS

The following section presents a sample calculation to show which quantities contribute most to the final measurement uncertainty. Several different samples of the industrial single crystal superalloy CMSX-4 Plus SLS [13] were processed using the NASA Marshall Space Flight Center (MSFC) electrostatic levitation (ESL) facility [12] to determine sample density as a function of temperature [14]. The thermograph depicting a typical time-temperature profile is shown in Figure 1. Note that in the figure, apparent temperature is reported in degrees Celsius because that is the reporting format from the pyrometer – these apparent values need to be subsequently corrected to true absolute temperature readings in Kelvin as part of the emissivity correction analysis

detailed below. To highlight pre- and post-analysis differences, the apparent temperature is presented in units of [°C] while absolute temperature is reported in [K]. The independent axis represents the relative time after data acquisition was initiated while the dependent axis is the apparent temperature as measured by a Mikron Infrared one-color pyrometer at a characteristic wavelength of 1.4 to 1.8 μm and an acquisition rate of 100 Hz. As shown in Table 1, to convert apparent temperature to real temperature the user must assume constant emissivity [15,16] over the temperature range of interest and assume that the sample stability is sufficient to maintain the pyrometer target view factor constant throughout the test. Assuming constant emissivity is appropriate for this material except for the temperature spike seen around the time interval $t \approx 50.5$ seconds where an oxide particle with high emissivity floated into the pyrometer target and then floated away. The temperature did not jump, but rather the emissivity change created an aphysical apparent temperature change. During the cooling period between $57 < t < 63$ seconds there were no emissivity changes and thus temperature could be calculated based on the relationship

$$T = \left[\left(\frac{1}{T_A}\right) + \left(\frac{1}{T_L} - \frac{1}{T_{LA}}\right)\right]^{-1} \tag{20}$$

Here, T represents the true temperature, T_A the apparent temperature, T_{LA} the apparent liquidus, and T_L the true liquidus – all in Kelvin. There is limited oscillatory motion indicated during the superheated liquid portion of the curve near 57 seconds but some limited translation is apparent during the deep undercooling of the liquid near 61 seconds. There is significant translation of the solid sample from 61 seconds onward thus indicating some stability issues with this sample. The dashed line shows the apparent liquidus following recalescence as defined by the data within the green rectangle and averaging this data yields $T_{LA} = 1619.63 \pm 4.39$ K for a sample size of $N = 97$ points. The apparent temperature at the red dot is shown for a data point near the liquidus temperature and conducting a deviation from the fit to the data over the range of points indicated by the red rectangle results in a value of $T_A = 1618.42 \pm 1.67$ K for a sample size of $N = 49$ points. The true temperature of this particular data point could then be evaluated based on the manufacturer's determination of the true liquidus at $T_L = 1607 \pm 5$ K [13].

After deriving mass from the pre-test and post-test weightings and deriving volume from calibrated digital video shadow images of sample projected area the results from three tests are shown in Figure 2. Two of the test samples showed very good agreement with significant data overlap while a third showed significant deviation.

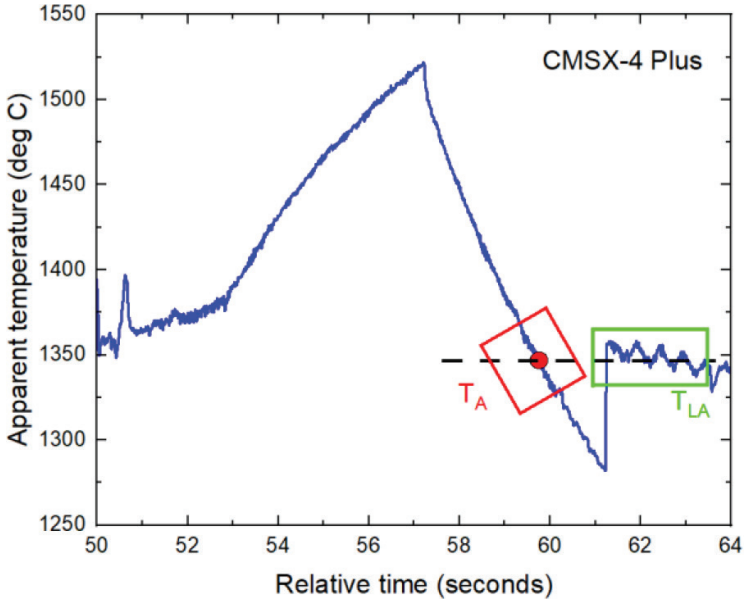

FIGURE 1
A typical melt cycle showing the time temperature profile during containerless processing of CMSX-4 Plus SLS alloy using electrostatic levitation.

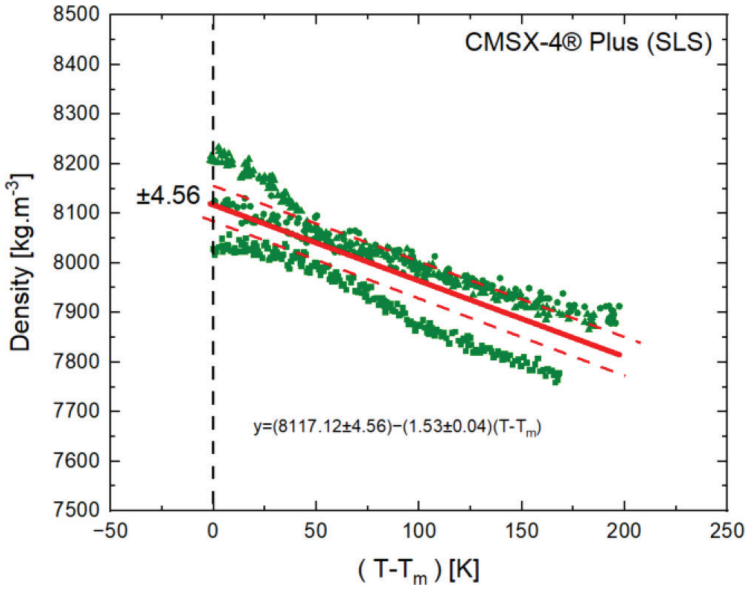

FIGURE 2
Experimental evaluation of density of CMSX-4 Plus SLS as a function of temperature.

Regression analysis: A simple regression analysis was performed on the combined dataset with the results shown in red on the Figure. The alloy liquidus represents the end of melting at $T_m = 1670$ K thus yielding $\Delta T = T_m - T = 0$. Reporting of the data at $x = 0$ indicates an uncertainty in intercept $u_b = \pm 4.56$ kg/m^3 (one sigma or 68% confidence). When calculating the data scatter, the uncertainty calculation yields $\sigma = \pm 59.57$ kg/m^3 for a combined regression uncertainty of $u_R = \sqrt{u_b^2 + \sigma^2} = 59.74$ kg/m^3. It is obvious that when taken alone, or even when combined, neither of these descriptions of uncertainty are visually able to characterize the spread of the data.

GUM analysis: To characterize uncertainty for each data point it is necessary to evaluate the uncertainty in the two derived quantities, density and temperature separately. Once temperature uncertainty is known, the slope is used to determine the contribution to uncertainty in density by uncertainty in temperature as outlined in the discussion for Equation 12.

Uncertainty in the derived density function has two components, mass and volume. Uncertainty in mass includes two contributions, uncertainty due to calibration of the scale used to measure the sample mass $[u_c(m_{init})/m = 0.1\mu g / 40\mu g = 0.25\%]$ and mass loss during testing due to evaporation $[u_c(m_{evap})/m = 0.3\mu g / 40\mu g = 0.75\%]$. Since both measurements are made using the same apparatus, we assume there may be some correlation. If they were uncorrelated, then with $r = 0$ from Equation 16 $[u_c(m)/m = \sqrt{(0.25\%)^2 + (0.75\%)^2} = 0.79\%]$. If perfectly positively correlated, then with $r = 1$ from Equation 17 $[u_c(m)/m = \sqrt{(0.25\% + 0.75\%)^2} = 1.00\%]$. If perfectly negatively correlated, then with $r = -1$ from Equation 18 $[u_c(m)/m = \sqrt{(0.25\% - 0.75\%)^2} = 0.50\%]$. Although the component due to calibration and the component due to drift are both most likely positive, since the uncertainty component from measurement resolution is uncorrelated and dominates either of the other two uncertainties, without further information we *could* be justified in assuming that $r = 0$. But since we wish to be conservative, we will assume $r = 1$ to maximize the uncertainty contribution from measurement of mass.

Volume is derived from sample radius which, in turn is derived from observations on the number of pixels in a projected video image $[u_c(px_{exp})/px_{exp} = 3px/335px = 0.90\%]$ which require calibration $[u_c(px_{cal})/px_{cal} = 1px/335px = 0.30\%]$ using a calibration sphere machined to extremely tight tolerance $[u_c(r_{cal})/r_{cal} = 0.0375\ \mu m / 20\ \mu m = 0.188\%]$ [17]. Since the measurement during the experiment and during calibration is done using the same apparatus, we assume there may be some correlation. For $r = 0$, $r = 1$, and $r = -1$ the resulting overall uncertainties are 0.96%, 1.21%, and 0.63%, respectively. Again, to be conservative, we will assume $r = 1$. These contributions are shown below in Table 2, presented in the coefficient of variation format from Equation 19:

TABLE 2
Uncertainty in derived functions based on uncertainty in inputs

Function	Inputs		Uncertainty
$\rho = [m / V]$	$x_1 = m$	$\partial\rho / \partial m = 1 / V$	$\left[\frac{V}{m}\right]^2 \left(\frac{1}{V}\right)^2 u^2(m) = \left(\frac{u_c(m)}{m}\right)^2 \quad \left[\frac{V}{m}\right]^2 \left(-\frac{m}{V^2}\right)^2 u^2(V) = \left(\frac{u_c(V)}{V}\right)^2$
	$x_2 = V$	$\partial\rho / \partial V = -m / V^2$	
	$u_c(m) / m = 1.00\%$	$r = 0$ (derived	$\frac{u_c(\rho)}{\rho} = \sqrt{\frac{u^2(m)}{m^2} + \frac{u^2(V)}{V^2}} = 3.76\%$
	$u_c(V) / V = 3.63\%$g	m & V uncorrelated)	
$m = [m_{init} - m_{evap}]$	$x_1 = m_{init}$	$\partial m / \partial m_{init} = 1$	$\left[\frac{1}{m}\right]^2 (1)^2 u^2(m_{init}) = \left(\frac{u(m_{init})}{m_{init}}\right)^2 \quad \left[\frac{1}{m}\right]^2 (-1)^2 u^2(m_{evap}) = \left(\frac{u(m_{evap})}{m_{evap}}\right)^2$
	$x_2 = m_{evap}$	$\partial m / \partial m_{evap} = -1$	
	$u_c(m_{init}) / m = 0.25\%$	Worst case assume	$\frac{u_c(m)}{m} = \sqrt{\left(\frac{u(m_{init})}{m_{init}} + \frac{u(m_{evap})}{m_{evap}}\right)^2} = 1.00\%$
	$u_c(m_{evap}) / m = 0.75\%$	$r = 1$ for m_{init} & m_{evap}	
$V = \left[\frac{4}{3}\pi r^3\right]$	$x_1 = r$	$\partial V = 4\pi r^2 \, \partial r$	$\frac{u_c(V)}{V} = \sqrt{\sqrt{\left[\frac{1}{V}\right]^2 \left(3\frac{V}{r}\right)^2 u_c{}^2(r)}}$
	$u_c(r) / r = 1.21\%$	$\partial V / V = 3\partial r / r$	
			$= 3\frac{u_c(r)}{r} = 3.63\%$

Function	Inputs		Uncertainty
$r = \left[px_{exp} \dfrac{r_{cal}}{px_{cal}} \right]$	$x_1 = px_{exp}$	$\partial r / \partial px_{exp} = \dfrac{r_{cal}}{px_{cal}}$	$\left[\dfrac{px_{cal}}{px_{exp} r_{cal}}\right]^2 \left(\dfrac{r_{cal}}{px_{cal}}\right)^2 u^2\left(px_{exp}\right) = \left(\dfrac{u\left(px_{exp}\right)}{px_{exp}}\right)^2$
	$x_2 = px_{cal}$	$\partial r / \partial px_{cal} = -px_{exp} \dfrac{r_{cal}}{px_{cal}^{\ 2}}$	$\left[\dfrac{px_{cal}}{px_{exp} r_{cal}}\right]^2 \left(-px_{exp} \dfrac{r_{cal}}{px_{cal}^{\ 2}}\right)^2 u^2\left(px_{cal}\right) = \left(\dfrac{u\left(px_{cal}\right)}{px_{cal}}\right)^2$
	$x_3 = r_{cal}$	$\partial r / \partial r_{cal} = \dfrac{px_{exp}}{px_{cal}}$	$\left[\dfrac{px_{cal}}{px_{exp} r_{cal}}\right]^2 \left(\dfrac{px_{exp}}{px_{cal}}\right)^2 u^2\left(r_{cal}\right) = \left(\dfrac{u\left(r_{cal}\right)}{r_{cal}}\right)^2$
	$u_c\left(px_{exp}\right) / px_{exp} = 0.90\%$	Worst case assume	
	$u_c\left(px_{cal}\right) / px_{cal} = 0.30\%$	$r = 1$ for px_{cal} & px_{exp}	$\dfrac{u_c(r)}{r} = \sqrt{\left(\dfrac{u\left(px_{exp}\right)}{px_{exp}} + \dfrac{u\left(px_{cal}\right)}{px_{cal}}\right)^2 + \left(\dfrac{u\left(r_{cal}\right)}{r_{cal}}\right)^2} = 1.21\%$
	$u_c\left(r_{cal}\right) / r_{cal} = 0.188\%$		
$T = \left[\left(\dfrac{1}{T_A}\right) + \left(\dfrac{1}{T_L} - \dfrac{1}{T_{LA}}\right)\right]^{-1}$	$x_1 = T_A$	$\dfrac{\partial(T)}{\partial(T_A)} = -\left[\left(\dfrac{1}{T_A}\right) + \left(\dfrac{1}{T_L} - \dfrac{1}{T_{LA}}\right)\right]^{-2} \cdot \left[-T_A^{-2}\right] = \left(\dfrac{T}{T_A}\right)^2$	$\left[\dfrac{1}{T}\right]^2 \left(\left(\dfrac{T}{T_A}\right)^2\right)^2 u^2(T_A) = \dfrac{T^2}{T_A^{\ 2}} \left(\dfrac{u(T_A)}{T_A}\right)^2$
	$x_2 = T_L$	$\dfrac{\partial(T)}{\partial(T_L)} = -\left[\left(\dfrac{1}{T_A}\right) + \left(\dfrac{1}{T_L} - \dfrac{1}{T_{LA}}\right)\right]^{-2} \cdot \left[-T_L^{-2}\right] = \left(\dfrac{T}{T_L}\right)^2$	$\left[\dfrac{1}{T}\right]^2 \left(\left(\dfrac{T}{T_L}\right)^2\right)^2 u^2(T_L) = \dfrac{T^2}{T_L^{\ 2}} \left(\dfrac{u(T_L)}{T_L}\right)^2$
	$x_3 = T_{LA}$	$\dfrac{\partial(T)}{\partial(T_{LA})} = -\left[\left(\dfrac{1}{T_A}\right) + \left(\dfrac{1}{T_L} - \dfrac{1}{T_{LA}}\right)\right]^{-2} \cdot \left[T_L^{-2}\right] = -\left(\dfrac{T}{T_{LA}}\right)^2$	$\left[\dfrac{1}{T}\right]^2 \left(\left(-\dfrac{T}{T_{LA}}\right)^2\right)^2 u^2(T_{LA}) = \dfrac{T^2}{T_{LA}^{\ 2}} \left(\dfrac{u(T_{LA})}{T_{LA}}\right)^2$
	$u_c\left(T_A\right) / T_A = 0.10\%$		
	$u_c\left(T_L\right) / T_L = 0.30\%$	Worst case assume	$\dfrac{u_c(T)}{T} = T\sqrt{\left(\dfrac{1}{T_A}\left(\dfrac{u(T_A)}{T_A}\right) + \dfrac{1}{T_{LA}}\left(\dfrac{u(T_{LA})}{T_{LA}}\right)\right)^2 + \dfrac{1}{T_L^{\ 2}}\left(\dfrac{u(T_L)}{T_L}\right)^2} = 0.49\%$
	$u_c\left(T_{LA}\right) / T_{LA} = 0.27\%$	$r = 1$ for T_A & T_{LA}	

(*Continued*)

TABLE 2 (*Continued*)

Function	Inputs	Uncertainty
$\rho_x = \rho_o + \frac{d\rho}{dT}(T - T_m)$ $\Delta T = (T - T_m)$	$x_1 = T$ $\quad \partial\rho_x / \partial T = d\rho / dT$ $x_2 = d\rho / dT$ $\quad \partial\rho_x / \partial (d\rho / dT) = \Delta T$ at $T = T_m$ (reference temperature) first term only $\Delta T = 0$ and $\rho_x = \rho_o$ need slope $\left(\frac{d\rho}{dT}\right) = -1.53$ kg/m^{3}K at $T \neq T_m$ (general case) both terms important need $u\left(\frac{d\rho}{dT}\right) = s_b = 0.04$ kg/m^{3}K In either case, $r = 0$ (derived ρ & T uncorrelated)	$\frac{u_x(\rho_x)}{\rho_x} = \sqrt{\left[\frac{1}{\rho_x}\right]^2 \left(\frac{d\rho}{dT}\right)^2 u^2(T) + \left[\frac{1}{\rho_x}\right]^2 (\Delta T)^2 u^2\left(\frac{d\rho}{dT}\right)}$ $= \left[\frac{1}{\rho_x}\right] \sqrt{\left[\frac{d\rho}{dT} \cdot u(T)\right]^2 + \left[\Delta T \cdot u\left(\frac{d\rho}{dT}\right)\right]^2}$ at $T = T_m$ $\quad \frac{u_x(\rho_o)}{\rho_o} = 0.15\%$

Table 2 also shows the uncertainty in temperature based on Equation 20. Two Type A evaluations are done based on Figure 1 where [u_c (T_A) / T_A = 1.67/1618.42 = 0.10%] and [u_c (T_{LA}) / T_{LA} = 4.39/1619.63 = 0.27%] augmented by the Type B evaluation from the alloy supplier [u_c (T_L) / T_L = 5/1607 = 0.31%]. Since T_A and T_{LA} were both evaluated from the same pyrometer then the readings may be correlated. For a data point where the corrected absolute temperature T = 1668.71 K such that the sample is slightly undercooled and ΔT = –1.29K, for r = 0, r = 1, and r = –1 the resulting overall uncertainties in temperature are 0.42%, 0.49%, and 0.35%, respectively. Again, to be conservative, we will assume r = 1. As seen for data presented in Table 2, this results in a precision of ± 8.15 K representing the temperature error bar at the liquidus.

The contribution to uncertainty in density by uncertainty in temperature is shown in the last row of Table 2. Here, the uncertainty has two contributions. First, there is contribution from the derived temperature uncertainty converted to uncertainty in density using the regression slope m. Second, there is a correction based on the product of the offset from the intercept at $\Delta T = 0$ and the potential deviation of the regression slope $u(\partial\rho / \partial T) = s_m$. In the special case where $\Delta T = 0$ (at the liquidus) the second term need not be considered. Based on previously discussed values, for the slightly undercooled sample the error in density due to uncertainty in temperature $u_x(\rho_o) / \rho_o$ becomes 0.13%, 0.15%, and 0.11% for correlation values of r = 0, r = 1, and r = –1 respectively.

4 DISCUSSION

Literature property measurement precision is commonly reported based solely on regression analyses. [4] The dataset presented in this paper was specifically selected to highlight the lack of rigor that this imparts. The uncertainty in intercept u_b = 4.56 kg/m^3 from Equation 5 fails to properly capture the visually apparent data scatter in Figure 2. When adding the regression deviation σ = 59.57 kg/m^3 from Equation 9 the overall regression uncertainty still inadequately describes the scatter. Refer to the Appendix for a numerical discussion of what factors influence the limits of this approach.

It is obvious that to properly quantify uncertainty, the individual data point error bars on derived quantities must be included. This can be accomplished using the GUM approach. When calculating uncertainty in density, which is seen in Table 2 to be 3.76% for this dataset, the uncertainty in mass at 1.00% is dominated by the uncertainty in volume at 3.63%. Delving deeper, the most significant uncertainty is in the measurement of radius during the experiment. This result is to be expected as the molten sample may exhibit deformation, rotation or translation. The analysis of the coefficient of variability for all inputs that result in the derived calculation of density thus provides the

researcher with information on prioritizing how the measurement technique might be improved in future experiments. And, when properly documented and reported, it gives modelers the ability to compare techniques.

Similarly for the uncertainty in temperature, the Type B uncertainty in liquidus from the alloy supplier and Type A uncertainty in apparent liquidus are of comparable magnitude. The uncertainty in apparent temperature is significantly lower than uncertainty in apparent liquidus as seen in Figure 1 where sample translation oscillations following recalescence increased such that the pyrometer target view factor was negatively influenced. The sinusoidal character of the signal is due to consistent, repeated changes in view factor as the pyrometer target is aligned with the sample center and then the edge and back to center. To improve precision, a researcher could report that data where translation was greater than some specified limit was omitted due to poor experimental conditions. This avoids "cherry-picking" of data as the omission of a limited set of data can be numerically justified.

The above discussion highlights selection of the value for the correlation r between the apparent temperature and the apparent liquidus. If we assume that the correlation between signal inputs was perfect and $r = 1$ then as T_{LA} goes up then T_A would go up. Two sinusoidal plots would emerge, both with a common frequency and phase shift but with potentially different amplitudes. The amplitude uncertainty would be accounted for during evaluation of the deviation from goodness of fit σ and thus error bars would capture only the scatter about the sinusoidal shape and not the time-averaged scatter relative to an individual measurement. But each dataset is taken at a different time interval, and the sample motion is thus perfectly non-correlated because phase shift and frequency are not synchronized. Note that the contribution from pyrometer calibration and from drift would still remain correlated and the value of the Pearson correlation coefficient would in practice be bounded by $0 \leq r \leq 1$. This equates to a resulting temperature precision shift between $\pm\ 7.06 < u_c(T) < \pm\ 8.15$ K and our selection of an assumed worst case such that $r = 1$ influences the density calculation only slightly given that other GUM uncertainties dominate.

Selection of a worst case correlation coefficient r does become important when considering the combination of all uncertainties. In the above example, once the uncertainty associated with the two contributions from regression (scatter and regression fit) are combined with the uncertainty associated with the two contributions from quantities using GUM (respective error bars on derived density and the contribution from derived temperature to density) the resulting density precision for $r = 0$, $r = 1$ and $r = -1$ shifts significantly from $\pm$ 244, $\pm$ 306, and $\pm$ 159 kg/m^3, respectively. Comparison of the relative contributions to the overall uncertainty from each of the four sources shows respective values of $\pm$ 60, $\pm$ 5, $\pm$ 305, and $\pm$ 12 kg/m^3 from scatter, fit, error bars on density, and error bars on temperature, respectively. Obviously to improve test precision it behooves the investigator to concentrate efforts on error bars on density which were previously noted to be dominated by

uncertainty in measurement of volume through uncertainty in the video evaluation of sample radius.

In order to visualize how the results from a new set of experimental measurements of a particular material property compare to previous literature results, a Measurement Accuracy and Precision (MAP) plot can be generated. The x-axis in a MAP plot represents the "Measurement Error" [7] of the new result μ_{ref} compared to any other previous reference literature results μ_i. As seen in Equation 21, a positive value shows that the literature value was higher than the new value while a negative value shows the opposite. The new data set serves as a reference for comparison, and as such it has a deviation of zero. The y-axis plots the coefficient of variation for a given data set based on the baseline value and associated absolute uncertainty, μ and σ respectively, as defined in Equation 22. Points are generated for each of the i data sets (x_i, y_i) using the following definitions.

$$x_i = \Delta_i = \frac{\mu_i - \mu_{ref}}{\mu_{ref}} \tag{21}$$

$$y_i = C_i = \frac{|\sigma_i|}{\mu_i} \tag{22}$$

Figure 3 shows such a comparison of facilities for several pure metals. Here, pure elemental Gold (Au) Zirconium (Zr) and Platinum (Pt) were tested using a variety of experimental levitation platforms to compare facility performance on different molten elements at their respective melting points. For these plots, deviation from literature value were calculated by comparing the relevant measurand properties as the baseline reference values to other reported literature values as listed in Table 3. Since the errors associated with the literature values were not exhaustively reported, a direct comparison between them and the measured properties would not convey the complete idea and thorough grasp of the newly reported values by encompassing all relevant aspects of uncertainties. Hence, the MAP plot remains a useful systematic tool towards reporting the newer measurement values while highlighting the variation of the previously reported values.

This visualization tool can be incredibly valuable to researchers specifically during ICME simulation and process optimization of welding or of layer-by-layer additive manufacturing. Modeling of the distribution of surface temperature in these surface tension-controlled processes, where the melt pool surface-shape directly affects understanding of Marangoni flow or thermocapillary convection caused by surface tension variation [27], can enable researchers to predict safe processing windows and potentially reduce the distribution of defect structures. The spatial variation of properties can be heavily influenced by the concentration of surface-active elements such as sulfur or oxygen on the melt pool surface. Often, a robust process of lower performance is better than an optimized performance which is highly

sensitive to minor variations in input parameters. Modelers can embrace use of Uncertainty Quantification (UQ) to guide process development.

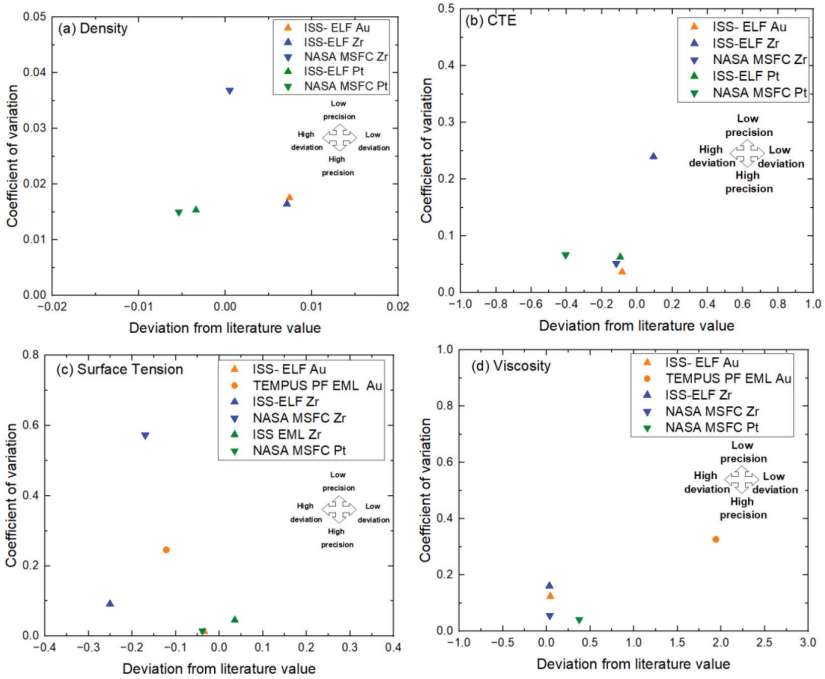

FIGURE 3
Measurement Accuracy and Precision (MAP) plot for pure elements at T_m (a) density, (b) coefficient of thermal expansion, (c) surface tension and (d) viscosity

TABLE 3
Reference values for evaluation of MAP plots

Element	Source	ρ_{ref} [10^3 kg·m^{-3}]	CTE_{ref} [10^{-5} K^{-1}]	σ_{ref} [N·m^{-1}]	μ_{ref} [mPa·s]
Au	ISS-ELF	1.72 [9]	7.60 [9]	1.11 [9]	5.6 [9]
	TEMPUS PF EML	–	–	1.01 [9]	10.65 [9]
	Literature	1.72 [18]	8.30 [19]	1.15 [20]	5.36 [21]
Zr	ISS-ELF	6.15 [10]	4.74 [10]	1.086 [10]	4.9 [10]
	MSFC ESL	6.11 [10]	3.79 [10]	1.20 [10]	5.03 [10]
	ISS EML	6.55	–	1.50 [10]	–
	Literature	6.11 [22]	4.60 [23]	1.45 [23]	4.7 [24]
Pt	ISS-ELF	1.92 [8]	10.9 [8]	–	–
	MSFC ESL	1.9 [8]	7.2 [8]	1.73 [8]	6.63 [8]
	Literature	19.3 [25]	5.0 [26]	1.80 [26]	4.82 [26]

Additionally, it allows comparison of the performance of a particular material in different facilities – guiding the selection of a specific facility for future testing on a specific material. In one example, the MAP plot from Figure 3(c) demonstrates that the surface tension data measured from ISS-ELF is of higher precision compared to the values measured from NASA MSFC ESL facility due to more prominent cases of oxidation during. Utilizing higher precision Zr surface tension data from ISS-ELF is going to contribute to lower propagation of error during modelling compared to lower precision surface tension from NASA MSFC. In another example, the MAP plots from Figure 3(d) shows higher precision of viscosity data for Au in ISS-ELF due to extended microgravity condition and controlled frequency sweeps compared to TEMPSU EML data from parabolic flight data due to possible impact of turbulent flow in viscosity.

Thus, by pre-utilizing MAP plots, researchers can formulate limits based on conscious choices of simulation parameters and thereby produce process boundaries to mitigate risks on predictions of optimized parameters.

5 CONCLUSIONS

It is critical that researchers clearly report how uncertainty is evaluated during any specific measurement program. This enables users to critically define confidence in measured properties, but more importantly it also provides documentation of measurement ranges and can highlight which part of the measurement protocol imparts the most potential error.

Uncertainty has four components. The two from standard regression analyses involve evaluation of uncertainty in slope and intercept and uncertainty in the deviation of the data from the proposed fit (ie. the data scatter). The two from derived quantities, using GUM techniques, involve uncertainty in the error bars for a specific data point – one for the independent and one for the dependent variables. All four must be taken into consideration when documenting and reporting experimental measurements.

The use of a coefficient of variation approach allows researchers to compare which contributing derived quantity has the most impact on the final result. Because this involves comparison of dimensionless quantities, all input functions may be compared simultaneously with the results representing a “percent deviation” for any given quantity. This guides the experimentalist in determining how to improve the measurement technique or modify the hardware to improve precision.

Measurement accuracy, involving both measurement trueness and measurement precision from any dataset, can be conveniently displayed using MAP plots. Using this tool, literature data can be compared to new set of measurements. This provides users with the ability to define the relative accuracy of the new results in parallel with a comparison of the precision across material families or across different experimental platforms or testing techniques.

REFERENCES

[1] Cowles, B.A., Backman, D.G. and Dutton, R.E. "Update to recommended best practice for verification and validation of ICME methods and models for aerospace applications", *Integr Mater Manuf Innov* **4**, 16–20 (2015). https://doi.org/10.1186/s40192-014-0030-8

[2] Hashemi S.M., Parvizi S., Baghbanijavid H., Tan A.T.L., Nematollahi Md., Ramazani A., Fang N.X., Elahinia Md., "Computational modelling of process–structure–property–performance relationships in metal additive manufacturing: a review". *Int.l Mater. Rev.*; **67**, 1–46(2022). https://doi.org/10.1080/09506608.2020.1868889

[3] O'Connor A., Littles L., Richter B., Glaessgen E., Karma A., Matson D.M., Voorhees P., Michael F., Rupp B., SanSoucie M., Sowards J., West J., Weber G.R., Pribe J.D., Yamakov V., Yeratapally S.R., Cole V., and Waxman R., "Reduced gravity and microgravity Integrated Computational Materials Engineering (ICME)", NASA Scientific and Technical (STI) – Program Technical Memorandum Report NASA/TM−20250000717 (2025) 1–73.

[4] Matson D.M., Watanabe M., Pottlacher G., Lee G.W. and Fecht H.-J., "Thermophysical Property Measurement: A Call to Action", *International Journal of Microgravity Science and Application*, 33[3] (2016), 330301 1–7. https://doi.org/10.15011/ijmsa.33.330304

[5] Budynas, R.G. and Nisbett, J.K., Shigley's Mechanical Engineering Design, 9th edition, McGraw-Hill, NY NY (2011) 992–995.

[6] Working Group 1 of the Joint Committee for Guides in Metrology [JCGM/WG1], Evaluation of measurement data: guide to the expression of uncertainty measurements, JCGM 100:2008 (2008).

[7] Working Group 2 of the Joint Committee for Guides in Metrology [JCGM/WG2], International vocabulary of basic and general terms in metrology (VIM). JCGM 200:2012, 3rd Eds. (2012).

[8] Nawer, J., Ishikawa, T., Oda, H., Koyama, C., and Matson, D.M., "Uncertainty quantification of thermophysical property measurement in space and on earth: A study of liquid Platinum using electrostatic levitation", *Journal of Astronomy and Space Science* **40** [3] (2023), 93–100. https://doi.org/10.5140/JASS.2023.40.3.93

[9] Nawer, J., Ishikawa, T., Oda, H., Saruwatari, H., Koyama, C., Xiao, X., Schneider, S., Kolbe, M., and Matson, D. M., "Uncertainty analysis and performance evaluation: a measurement of thermophysical properties of liquid Au in microgravity", *npj Microgravity* **9:38** (2023), 1–9. https://doi.org/10.1038/s41526-023-00277-0.

[10] Nawer, J. and Matson, D.M., "Quantifying facility performance during thermophysical property measurement of liquid Zr using Electrostatic Levitation", *High Temperatures High Pressures* **52** [2] (2023) 123–138. https://doi.org/10.32908/hthp.v52.1315

[11] Nawer J., Xiao X., Sansoucie M.P., and Matson D.M., "Effect of mass evaporation on measurement of liquid density of Ni-based superalloys using ground and space levitation techniques", *High Temperatures High Pressures* **49** [1–2] (2020), pp. 17–29. https://doi.org/10.32908/hthp.v49.839

[12] Hyers, R.W. and Rogers, J.R. "A Review of Electrostatic Levitation for Materials Research" *High Temperature Materials and Processes*, **27** [6], (2008) 461–474. https://doi.org/10.1515/HTMP.2008.27.6.461

[13] Wahl, J.B., Harris, K., "CMSX-4 Plus single crystal alloy development, characterization, and application development", in Superalloys 2016: Proceedings of the 13th International Symposium on Superalloys, eds. Hardy M., Huron H., Glatzel, U. Griffin B., Lewis B., Rae C, Seetharaman V., Tin, S. TMS (2016) 25–33.

[14] Nawer, J., Ishikawa, T., Oda, H., Koyama, C., Pichler, P., Leitner, T., Pottlacher, G., and Matson, D.M., "A quantitative comparison of thermophysical property measurement of CMSX-4® Plus (SLS) in microgravity and terrestrial environments", *High Temperatures High Pressures* **52** [2] (2023) 323–339. https://doi.org/10.32908/hthp.v52.1407

[15] Alaruri, S., Bianchini, L., Brewington, A., "Effective spectral emissivity measurements of superalloys and YSZ thermal barrier coating at high temperatures using a 1.6 m single wavelength pyrometer" *Optics and Lasers in Engineering* 30 (1998) 77–91. https://doi.org/10.1016/S0143-8166(97)00108-5

[16] Mohr, M., Wunderlich, R., Dong, Y., Furrer, D., Fecht, H.-J., "Thermophysical Properties of Advanced Ni-Based Superalloys in the Liquid State Measured on Board the Interna-

tional Space Station" Advanced Engineering Materials **22** [4] (2020) 1901228 1–10. https://doi.org/10.1002/adem.201901228

[17] Bradshaw, R.C., Warren, M.E., Rogers, J.R., Rathz, T.J., Gangopadhyay, A.K., Kelton, K.F., Hyers R.W., "Containerless measurements of thermophysical properties of $Zr_{54}Ti_8Cu_{20}Al_{10}Ni_8$", *Ann. NY Acad. Sci.* **1077** (2006) 63–74. https://doi.org/10.1196/annals.1362.058

[18] Kaschnitz, E., Nussbaumer, G., Pottlacher, G., Jager, H., "Microsecond-resolution measurements of the thermophysical properties of liquid gold", *Intl J Thermophys.*, **14**, (1993) 251–257. https://doi.org/10.1007/BF00507812

[19] Paradis, P.F., Ishikawa, T. and Koike, N., "Density of liquid gold measured by a non-contact technique"*Gold Bulletin*, **41**, 1–4 (2008). https://doi.org/10.1007/BF03214876

[20] Egry, I., Lohöfer, G., Jacobs, G., "Surface tension of liquid metals: results from measurements on ground and in space", *Phys. Rev. Lett.* **75**: 4043 (1995). https://doi.org/10.1103/PhysRevLett.75.4043.

[21] Ofte, D., "The viscosity of liquid uranium, gold, and lead", *J. Nucl. Mater*., **22**, (1967) 28–32. https://doi.org/10.1016/0022-3115(67)90105-5

[22] Korobenko, V. N. and Savvatimskii, A. I, "Temperature dependence of the density and electrical resistivity of liquid Zirconium up to 4100 K", 39, (2001), 525–531. https://doi.org/10.1023/A:1017932122529

[23] Paradis, P.-F. and Rhim, W.K., "Thermophysical properties of zirconium at high temperature", *J. Mater. Res.* **14 [9]**, (1999) 3713–3719. https://doi.org/10.1557/JMR.1999.0501

[24] Ishikawa, T. and Paradis, P.-F., "Thermophysical properties of molten refractory metals measured by an electrostatic levitator", *J. Electron. Mater*., **34**, (2005) 1526–1532. https://doi.org/10.1007/s11664-005-0160-z

[25] Hixson R.S. and Winkler M.A., "Thermophysical properties of liquid platinum", *Int. J. Thermophys.*, **14**, [3], (1993) 409–416. https://doi.org/10.1007/BF00566040

[26] Ishikawa, T., Paradis, P.-F. and Koike, N., "Non-contact thermophysical property measurements of liquid and supercooled platinum", *Jpn. J. Appl. Phys.*, **45** [3A], (2006) 1719–1724. https://doi.org/10.1143/JJAP.45.1719

[27] Lee, Y. S. and Farson, D.F., "Surface tension-powered build dimension control in laser additive manufacturing process", *Int. J. Adv. Manuf. Technol.,* 85, (2016), 1035–1044. https://doi.org/10.1007/s00170-015-7974-5

Appendix – Evaluation of a simulated data set to illustrate limits of regression analysis

In the body of the paper, the dataset chosen for analysis was intentionally selected to show the need to evaluate experimental data uncertainty from both contributing components – quantification of the uncertainty relative to the physics-based functional relationship and the uncertainty in the derived quantities. To better visualize the limits of using only a regression technique, two simulated datasets are presented.

In the first case, we conduct a simulation to determine uncertainty in regression slope and intercept as the standard deviation of the data increases. In Figure A-1(a), the frequency of the x-value is set to a constant frequency (number of data points per one arbitrary unit) $f = 100$ and the slope set to $m = –0.10$ and the intercept set to $b = 6$ at x = 0. The standard deviation is increased for each of four cases such that it spans the range $\sigma = (0.1, 0.5, 1.0,$ and $3.0)$ which causes an increase in uncertainty in slope and in intercept. Obviously, a higher data spread has higher uncertainty as seen in Figure A-1(b). In summary, an evaluation of σ captures the magnitude of random scatter of the data

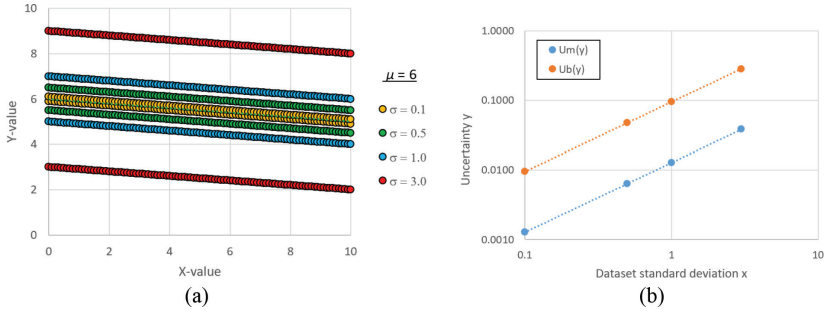

FIGURE A-1
Simulated dataset with varying standard deviation
(a) raw simulated data, (b) uncertainty in regression slope m and intercept b

In the second case, we conduct a simulation to determine uncertainty in regression slope and intercept as the number of data points increases. In Figure A-2(a), the frequency of the x-value is set to a constant $f = 100$ and the slope set to $m = –0.10$ while the value of the intercept is incremented over the range $b = (2, 4, 6, 8)$ to better separate each correlation visually. The standard deviation is increased for each of four cases such that it spans the range of $\sigma = (0.1, 0.5, 1.0,$ and $3.0)$ which causes a decrease in uncertainty in slope and in intercept as seen in Figure A-2(b). Since the standard deviation of the results is the same value for all datasets increasing the number of data points has no impact on σ and it successfully characterizes random scatter. In summary, the more data points considered, the more the regression intercept and slope uncertainty decreases and thus u_b captures goodness-of-fit.

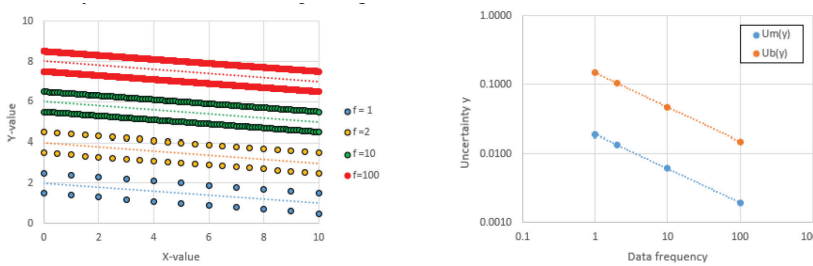

Figure A-2
Simulated dataset with varying standard deviation
(a) raw simulated data, (b) uncertainty in regression slope *m* and intercept *b*

To accomplish a proper regression the first case shows we need to evaluate the deviation from the regression while the second case independently shows the confidence in that regression. Both are needed.